

# Comparing interpretation methods in mental state decoding analyses with deep learning models

Armin W. Thomas<sup>∇,∨,°</sup>, Christopher Ré<sup>⊔,°</sup>, and Russell A. Poldrack<sup>∇,∨,°</sup>

<sup>∇</sup>Stanford Data Science, Stanford University, Stanford, CA, USA

<sup>∨</sup>Dept. of Psychology, Stanford University, Stanford, CA, USA

<sup>⊔</sup>Dept. of Computer Science, Stanford University, Stanford, CA, USA

<sup>°</sup>{athms,chrisre,russpold}@stanford.edu

May 2022

## Abstract

Deep learning (DL) methods find increasing application in mental state decoding, where researchers seek to understand the mapping between mental states (such as accepting or rejecting a gamble) and brain activity, by identifying those brain regions (and networks) whose activity allows to accurately identify (i.e., decode) these states. Once DL models have been trained to accurately decode a set of mental states, neuroimaging researchers often make use of interpretation methods from explainable artificial intelligence research to understand their learned mappings between mental states and brain activity. Here, we compare the explanations of prominent interpretation methods for the mental state decoding decisions of DL models trained on three functional Magnetic Resonance Imaging (fMRI) datasets. We find that interpretation methods that capture the model’s decision process well, by producing faithful explanations, generally produce explanations that are less in line with the results of standard analyses of the fMRI data, when compared to the explanations of interpretation methods with less explanation faithfulness. Specifically, we find that interpretation methods that focus on how sensitively a model’s decoding decision changes with the values of the input produce explanations that better match with the results of a standard general linear model analysis of the fMRI data, while interpretation methods that focus on identifying the specific contribution of an input feature’s value to the decoding decision produce overall more faithful explanations that align less well with the results of standard analyses of the fMRI data.

Deep learning (DL) methods have celebrated immense successes in many areas of research and industry over recent years, often outperforming conventional machine learning approaches (Goodfellow et al., 2016, LeCun et al., 2015). This success is generally attributed to their unparalleled ability to autonomously learn versatile representations of complex datasets, allowing them to associate a target signal with varying patterns in minimally-preprocessed or raw data. Their empirical success has triggered interest in the application of DL methods to neuroimaging research, particularly, mental state decoding (Haynes and Rees, 2006). Here, researchers aim to identify how specific mental states (e.g., answering questions about a prose story or math problem) are represented in the brain, by identifying brain regions (or networks of brain regions) whose activity supports accurate identification (i.e., decoding) of these mental states. To this end, researchers train predictive models to accurately decode these states from measured brain activity.

While neuroimaging researchers are currently still debating the conditions under which DL models are in fact advantageous (or necessary) over more conventional machine learning approaches (e.g., Abrol et al., 2021, Dadi et al., 2019, Schulz et al., 2020), the field is experiencing an increase in their application to mental state decoding (e.g., Mensch et al., 2021, Plis et al., 2014, Thomas et al., 2019, VanRullen and Reddy, 2019, Wang et al., 2020, Zhang et al., 2021). To overcome

the un-interpretability of DL models (Rudin, 2019), which disguise their learned mappings between input data and decoding decisions through many non-linear transforms of the data, neuroimaging researchers often make use of interpretation methods from explainable artificial intelligence research (XAI; Doshi-Velez and Kim, 2017, Samek et al., 2021), which seek to provide insights into the models’ learned mappings between input data and decoding decisions. From the wealth of existing interpretation methods (Gilpin et al., 2018, Linardatos et al., 2021), neuroimaging researchers most often utilize attribution (i.e., heatmapping) methods, which seek to attribute a relevance to each feature value of an input for the resulting decoding decision of a DL model, resulting in a heatmap of relevance values (Samek et al., 2021). On a high level, the most prominent attribution methods in mental state decoding can be grouped into sensitivity analyses (e.g., Simonyan et al., 2014, Smilkov et al., 2017, Springenberg et al., 2015), reference-based attributions (e.g., Lundberg and Lee, 2017, Shrikumar et al., 2017, Sundararajan et al., 2017), and backward decompositions (e.g., Bach et al., 2015, Montavon et al., 2017). Sensitivity analyses, such as Gradient Analysis (Simonyan et al., 2014), attribute relevance to input features according to how sensitively a model’s decoding decision responds to the feature’s value. Reference-based attributions, such as DeepLift (Shrikumar et al., 2017) or Integrated Gradients (Sundararajan et al., 2017), in contrast, attribute relevance to input features by comparing the model’s response to its response to a reference input (often chosen to be neutral). Backward decompositions, such as Layer-wise relevance propagation (LRP; Bach et al., 2015), on the other hand, attribute relevance to input features by decomposing the decoding decision of a DL model in a backward pass through the model into the contributions of lower-level model units to this decision, up to the input space, where a contribution for each input feature can be defined.

Given the wealth of existing interpretation methods, researchers in neuroimaging interested in utilizing these methods are faced with the task of identifying a method that best-suites their research question at hand. Yet, in many cases, the explanations (i.e., attributions) of many interpretation methods are difficult to visually discern, making it challenging to compare and evaluate their quality. Further, it is currently unclear whether related empirical findings from computer vision (CV; Adebayo et al., 2018, Kindermans et al., 2019, Samek et al., 2017) or natural language processing (NLP; Ding and Koehn, 2021, Jacovi and Goldberg, 2020, Jain and Wallace, 2019) on the comparison of different interpretation methods generalize to neuroimaging data. There, researchers have often argued that reference-based attributions and backward decompositions are generally superior to sensitivity analyses, because they more faithfully capture the decision process of DL models. Yet, mental state decoding is distinct from most CV and NLP applications in that it aims to understand the mapping between input data (i.e., brain activity) and decoding targets (i.e., mental states), whereas the application of DL models in CV or NLP is mostly concerned maximal predictive performances. It thus remains an open question how prominent interpretation methods compare in providing insights into the underlying mapping between brain activity and mental states through the lens of trained DL models.

With this work, we seek to provide insights into these questions, by comparing the performance of prominent interpretation methods in a mental state decoding analysis of three functional Magnetic Resonance (fMRI) datasets. To this end, we first train DL models to accurately decode the mental states of each dataset and subsequently compare the quality of the interpretation method’s explanations of the models’ decoding decisions on three evaluation criteria: First, to understand how well the explanations align with the results of standard analyses of fMRI data, we compare the similarity of the explanations to the results of a standard general linear model (GLM; Friston et al., 1994) analysis of the fMRI data. We find that the explanations of sensitivity analyses are generally more similar to standard GLM contrast maps, when compared to the explanations of reference-based attributions and backward decompositions. In a second step, we then evaluate the faithfulness of the methods’ explanations, by testing whether they accurately identify those voxels of the input whose activity a model uses to decode its set of mental states. We find that the explanations of reference-based attributions and backward decompositions are generally more faithful

than those of sensitivity analyses. Lastly, we perform two sanity checks for the explanations of any attribution method, based on recent empirical work in machine learning (ML) research Adebayo et al. (2018), by testing whether the methods’ explanations are in fact sensitive to the characteristics of the analyzed data and model. By integrating findings from these three evaluations, we derive a set of specific recommendations for the application of interpretation methods in mental state decoding: If researchers are interested in understanding the decision process of a DL model, by identifying those parts of the input that are most important for the model’s decoding decision, we recommend the application of reference-based attributions, such as DeepLift (Shrikumar et al., 2017) and Integrated Gradients (Sundararajan et al., 2017), or backward decompositions, such as LRP (Bach et al., 2015), while we recommend sensitivity analyses, such as Gradient Analysis (Simonyan et al., 2014) and Guided Backpropagation (Springenberg et al., 2015), for situations in which researchers are more interested in understanding the mapping between brain activity and mental states and DL models are mainly used as a tool to capture this mapping.

# 1 Methods

## 1.1 Data

We analyzed fMRI data from three experiments in this study, namely, data from 44 randomly-selected individuals in the motor task of the Human Connectome Project (HCP; Van Essen et al., 2013), 44 randomly-selected individuals in the HCP’s working memory (WM) task, and 58 individuals in a pain and social rejection experiment published by Woo et al. (2014). We refer to these three datasets as "MOTOR", "WM", and "heat-rejection" in the following and provide a brief overview of their experiment tasks as well as details on the fMRI acquisition and preprocessing. For any further methodological details, we refer the reader to the original publication of each dataset (namely, Van Essen et al., 2013, Woo et al., 2014).

### 1.1.1 Experiment tasks

**Heat-rejection:** The heat-rejection dataset comprises fMRI data from two experimental tasks. In the social rejection task, individuals see head shots of their ex-partners or close friends in addition to a cue-phrase beneath each photo directing participants to think about how they felt during their break-up experience with the ex-partner or a specific positive experience with their friend. In the somatic pain task, individuals focus on a hot (painful) or warm (non-painful) stimulus that was delivered to their left forearm (the temperature was calibrated for each person). Each rejection trial begins with a 7 s fixation cross, followed by a 15 s presentation period of a photo (ex-partner or friend), a 5 s five-point affect rating period, and 18 s of a visuo-spatial control task in which individuals see an arrow pointing left or right and are asked to indicate in which direction the arrow is pointing. Heat trials are identical in structure to the rejection trials with the exception that individuals see a fixation cross during the 15 s thermal stimulation period (consisting of a 1.5-s temperature ramp up/down and 12 s at peak temperature) and subsequently use the five-point rating scale to report their experienced pain.

**MOTOR:** In the HCP’s motor task individuals see visual cues asking them to tap their left or right fingers, squeeze their left or right toes or move their tongue. The task is presented in blocks of 12 s, each including one movement type, preceded by 3 s cue. Two fMRI runs were collected for this task, each containing two blocks of tongue movements, four blocks of hand movements (two left, two right), and four blocks of foot movements (again, two left and two right) as well as three 15 s fixation blocks.

**WM:** As for the motor task, two fMRI runs were collected for the HCP’s WM task. Each run contains eight task (25 s each) and four fixation blocks (15 s each). In task blocks, individuals see images of one of four different stimulus types (body parts, faces, places or tools). Half of the task blocks use a 2-back working memory task (individuals are asked to respond “target” when the current stimulus is the same as the stimulus 2 back) while the other half uses a 0-back working memory task (a target stimulus is presented at the beginning of a block and individuals are asked to respond “target” whenever a stimulus matches the target). Each task block consists of 10 trials (2.5 s each). In each trial, a stimulus is presented for 2 s followed by a 0.5 s interstimulus interval. As we are not interested in identifying any effect of the N-back task condition on brain activity, we pool the data of the two N-back conditions.

### 1.1.2 FMRI data acquisition

**Heat-rejection:** Whole-brain EPI acquisitions were acquired on a 3T Siemens Trio system (Siemens) with a 12-channel receiver head coil using a T2\*-weighted functional EPI sequence with TR = 2,000 ms, TE = 29 ms, flip angle = 75, slice thickness = 3.5 mm, FOV = 24 cm (for further methodological details on fMRI data acquisition, see Woo et al., 2014).

**Human Connectome Project:** Whole-brain EPI acquisitions were acquired with a 32 channel head coil on a modified 3T Siemens Skyra with TR = 720 ms, TE = 33.1 ms, flip angle = 52 deg, BW = 2,290 Hz/Px, in-plane FOV = 208 x 180 mm, 72 slices, 2.0 mm isotropic voxels with a multi-band acceleration factor of 8. Two runs were acquired for each task, one with a right-to-left and the other with a left-to-right phase encoding (for further methodological details on fMRI data acquisition, see Uğurbil et al., 2013).

### 1.1.3 FMRI data preprocessing

**Human Connectome Project:** We preprocessed the fMRI data of the MOTOR and WM datasets with fmriprep (20.2.3; Esteban et al., 2019), without FreeSurfer Fischl (2012) surface preprocessing. A detailed description of all preprocessing steps can be found in Appendix A.1.1.

**Heat-rejection:** The data was preprocessed by the original authors (see Woo et al., 2014). The preprocessing included skull stripping with FSL’s Brain (realignment), 8mm FWHM Gaussian kernel smoothing, warping to the Montreal Neurological Institute template (with FMRIB’s Linear Image Registration Tool), temporal filtering using a band-pass filter between 0.009 and 0.08 Hz, and confound removal by regressing out the six head movement parameters (x, y, z, roll, pitch and yaw) and their first temporal derivatives, the top five principal components from the signal averaged in the white matter and ventricles, and frames that were identified as motion or intensity outliers.

## 1.2 Trial-level statistical parametric maps

All of our analyses were performed on trial-level statistical parametric maps (Friston et al., 1994) that were computed for each experiment trial in each dataset. Note that we refer to the resulting maps as trial-level blood-oxygen-level-dependent (BOLD) maps throughout the rest of the manuscript.

**Heat-rejection:** Voxel-wise statistical parametric maps for each trial were computed by the original authors by the use of SPM8 (see Woo et al., 2014). This analysis included task regressors corresponding to the 15 s photo or pain periods, the subsequent 5 s affect or pain rating period, and the 18 s period of the visuospatial control task (leaving the fixation cross period as an unmodelled

baseline). The task regressors were convolved with SPM8’s canonical haemodynamic response function (HRF) and temporally filtered with a high-pass filter of 180 s. In addition, confound regressors of no interest were included in the analysis representing indicator vectors for each run, a linear drift across time within each run, the six estimated head movement parameters for each run (x, y, z, roll, pitch and yaw; mean-centered) as well as their squares, derivatives, and squared derivatives, indicator vectors for outlier time points, and indicator vectors for the first two images of each run.

**Human Connectome Project:** Voxel-wise statistical parametric maps were computed separately for each experimental run of each individual by the use of Nilearn 0.9.0 (Abraham et al., 2014a). For each run, we included task regressors representing each of the trial types (body, face, place, tool for the WM task and left/right foot, left/right finger, and tongue for the MOTOR task), which we convolved with a standard Glover HRF (as implemented by Nilearn (Abraham et al., 2014a); again leaving the fixation periods as unmodelled baselines). In addition, counfound regressors of no interest were added to the analysis representing the six estimated head movement parameters (x, y, z, roll, pitch and yaw) as well as their squares, derivatives, and squared derivatives, the average signal of white matter and cerebrospinal fluid masks, the global signal, and a set of low-frequency regressors to account for slow signal drifts below 128 s.

### 1.3 Deep learning model

We use 3D-convolutional neural network architectures (3D-CNNs; LeCun et al., 1998) in this study, which are composed of a stack of 3D-convolution layers in addition to a dense output layer.

A 3D-convolution layer consists of a set of 3D-kernels  $w$  that each learn specific features of an input volume  $x$ . Each kernel  $k$  learns a volumetric feature that is convolved over the input, resulting in an activation map  $A^k$  for each kernel, indicating the presence of its learned feature at each spatial location of the input volume:  $A_{i,j,l}^k = g(\sum_{m=1}^M \sum_{n=1}^N \sum_{z=1}^Z w_{m,n,z}^k x_{i+m-1,j+n-1,l+z-1} + b^k)$ . Here,  $b^k$  and  $w^k$  represent the bias and weights of the kernel, while  $g$  represents the rectified linear unit activation function ( $g(x) = \max(0, x)$ ). The indices  $m$ ,  $n$ , and  $z$  index the row, column, and height of the 3D-convolution kernel, while  $i$ ,  $j$ , and  $l$  indicate the coronal (i.e., row), sagittal (i.e., column), and axial (i.e., height) dimension of the activation map  $A^k$ .

To make a decoding decision, we flatten the 3D-convolution feature maps  $A$  of the last convolution layer  $L$  and passes the resulting vector  $a$  through a dense softmax layer, to predict a probability  $p_c$  that input  $x$  represents mental state  $c$ :  $p_c = \sigma(b_c + \sum_i a_i \times w_{ic})$ , where  $b$  and  $w$  represent the layer’s bias and weights, while  $\sigma$  indicates the softmax function:  $\sigma(x)_j = \frac{e^{x_j}}{\sum_i e^{x_i}}$ .

Note that we train separate 3D-CNN models for each of the three fMRI datasets (see section 1.1). To determine the specific 3D-CNN configuration for each dataset, we perform a grid search over the number of convolutional layers, number of kernels per layer, and the kernels’ size (for details, see section 2.1). We also move all convolution kernels over their input at a stride size of 2, thus applying the kernels to every other value of a layer’s input.

#### 1.3.1 Training details

We train models with stochastic gradient descent and the ADAM optimizer (Kingma and Ba, 2017) for 40 training epochs, where one epoch is defined as an entire iteration over the training data. For each dataset, we further evaluate multiple learning rates, batch sizes, and dropout rates (Srivastava et al., 2014) in a standard grid search (see section 2.1).

## 1.4 Interpretation methods

We assume that the analyzed model  $f$  represents some function  $f(\cdot)$  mapping an input  $x \in \mathbb{R}^D$  to some output  $f(x) \in \mathbb{R}$ , such that:  $f(\cdot) : \mathbb{R}^D \rightarrow \mathbb{R}$ . In the following, we present a set of interpretation methods  $\eta(\cdot)$  that seek to provide insights into this mapping by attributing a relevance score  $r_d$  to each input feature  $d \in D$  quantifying its contribution to  $f(x)$ , such that:  $\eta(\cdot) : \mathbb{R} \rightarrow \mathbb{R}^D$ .

On a high level, the presented interpretation methods can be divided into sensitivity analyses, reference-based attribution methods, and backward decompositions. Sensitivity analyses quantify  $r$  by determining how sensitively  $f(x)$  responds to  $x$ . Reference-based attributions, in contrast, quantify  $r$  by contrasting the model’s response to a given input  $x$  to its response to a reference input  $b$ . Backward decompositions, on the other hand, quantify  $r$  by sequentially decomposing the model’s output  $f(x)$  in a backward pass through the model into the contributions of the lower-layer model units to the predictions, until the input space is reached and a contribution for each input feature can be defined.

**Gradient Analysis:** Gradient Analysis (Simonyan et al., 2014, Zurada et al., 1994) is the most commonly used sensitivity analysis and defines  $r_d$  as the derivative of  $f(x)$  with respect to the input  $x_d$ , such that:  $r_d = (\frac{\delta f(x)}{\delta x_d})^2$ . Relevance is thus assigned to those feature values to which  $f(x)$  responds most sensitively.

**SmoothGrad:** SmoothGrad (Smilkov et al., 2017) represents an extension of Gradient Analysis to account for sharp fluctuations of the derivative (i.e., gradient)  $\Delta f(x)$  at small scales, which can otherwise lead to noise in the resulting attributions. To this end, SmoothGrad repeatedly takes  $N$  random samples (we set  $N = 50$ ) from the neighborhood of  $x$ , by adding random Gaussian noise  $\mathcal{N}(0, \sigma^2)$  with standard deviation  $\sigma$  (we set  $\sigma = 1$ ) to  $x$ , and then averages over the resulting gradients to obtain relevances  $r$ :  $r = \frac{1}{N} \sum_1^N \Delta f(x + \mathcal{N}(0, \sigma^2))$ .

**InputXGradient:** InputXGradient (Shrikumar et al., 2017) represents another extension of Gradient Analysis, which multiplies the gradient  $\Delta f(x)$  by the input  $x$ , such that:  $r = \Delta f(x) \cdot x$ . The intuition behind this approach comes from linear models, where the product of input and model coefficient (here represented by the gradient) corresponds to the total contribution of the associated feature to the model’s output.

**Guided Backpropagation:** Guided Backpropagation (Springenberg et al., 2015) also represents an extension of Gradient Analysis that is tailored to CNNs using rectified linear unit (ReLU; Agarap, 2019) activation functions. It computes the gradient  $\Delta f(x)$ , but overrides gradients of ReLU activation functions such that only non-negative gradients are backpropagated, thereby preventing backward flow of negative gradients.

**Guided Gradient-weighted Class Activation Mapping (Guided GradCam):** Guided Gradient-weighted Class Activation Mapping (Guided GradCam) represents another variant of sensitivity analysis that is tailored to CNNs, by combining Guided Backpropagation with the GradCam (Selvaraju et al., 2017) technique. Specifically, GradCam first computes the gradient  $\Delta f(x)$  with respect to the  $k$  feature maps  $A$  of the convolutional layer  $L$  that is closest to the model’s output ( $\frac{\delta f(x)}{\delta A^k}$ ) and then global-average pools the resulting gradients to obtain an importance weight  $\alpha_k$  for each kernel  $k \in L$ :  $\alpha_k = \frac{1}{J \cdot Z} \sum_{j=1}^J \sum_{z=1}^Z \frac{\delta f(x)}{\delta A_{j,z}^k}$ . Conceptually,  $\alpha_k$  captures the importance of feature map  $A^k$  for the decoded mental state. Next, GradCam uses the importance weights to combine the activation maps  $A^k$  to an aggregate heatmap of relevances for each location of the feature maps  $r_A$ :  $r_A = \sigma(\sum_k \alpha_k^L \cdot A^k)$ , where  $\sigma$  represents the ReLU function ( $\sigma(x) = \max(0, x)$ ). Lastly, Guided GradCam upsamples the relevances  $r_A$  to the original input dimension

and multiplies them with the relevance attributions of an application of Guided Backpropagation to  $f(x)$  (see above), to obtain final relevances  $r_d$  for each feature  $d$  of the input.

**Integrated Gradients:** Integrated Gradients (Sundararajan et al., 2017) represents a reference-based attribution method that assigns relevance  $r$  by integrating the gradient  $\Delta f(x)$  along a linear trajectory in the input space, connecting the current input  $x$  to some neutral reference input  $b$ :  $r^b = (x - b) \cdot \int_{\alpha=0}^1 \frac{\delta f(b + \alpha(x-b))}{\delta x}$ . Integrated gradients thus assigns relevance to input features according to how much the model’s output changes when these features are scaled from the reference value to their current value. In our analyses, we chose two reference inputs, namely, an all-zero input  $b^0$  (as recommended in Sundararajan et al., 2017) as well as an average over all inputs in the analyzed dataset  $b^\mu$ , and averaged over both resulting attributions to obtain relevance values  $r$ :  $r = 0.5 \cdot r^0 + 0.5 \cdot r^\mu$ .

**Deep Learning Important FeaTures (DeepLift):** The Deep Learning Important FeaTures (DeepLift; Shrikumar et al., 2017) technique can be seen as both, a reference-based attribution method and a backward decomposition. Similar to Integrated Gradients, DeepLift determines relevances  $r$  by comparing model responses for a given input  $x \in \mathbb{R}^D$  to the model’s response to some neutral reference input  $b \in \mathbb{R}^D$ . To this end, DeepLift defines a contribution score  $C_{\Delta x_d \Delta f(x)}$ , which describes the response difference-from-reference  $\Delta f(x) = f(x) - f(b)$  that is attributed to the input difference-from-reference  $\Delta x_d = x_d - b_d$ . Note that  $\sum_d C_{\Delta x_d \Delta f(x)} = \Delta f(x)$ . To compute these contribution scores, DeepLift introduces the concept of multipliers  $m_{\Delta x_d \Delta f(x)}$ , which are defined as  $m_{\Delta x_d \Delta f(x)} = \frac{C_{\Delta x_d \Delta f(x)}}{\Delta x_d}$ , thus quantifying the contribution of  $\Delta x$  to  $\Delta f(x)$ , scaled by  $\Delta x$ . For any unit  $x^{(l)}$  in model layer  $l$  and any unit  $x^{(l-1)}$  in the preceding layer  $l-1$ , these multipliers can be computed as:  $m_{\Delta x_d^{(l-1)} \Delta f(x)} = \sum_j m_{\Delta x_d^{(l-1)} \Delta x_j^{(l)}} \cdot m_{\Delta x_j^{(l)} \Delta f(x)}$ , in line with the chain rule. Relevance  $r_d$  for input feature  $d$  can then be obtained by:  $r_d = C_{\Delta x_d \Delta f(x)} = \Delta x_d \cdot m_{\Delta x_d \Delta f(x)}$ . In its basic formulation, DeepLift uses two rules to compute contribution scores. The linear rule applies to dense and convolution layers, which compute  $a = w_0 + \sum_{i=1}^D w_i \cdot x_i$  (where  $w_0$  and  $w$  indicate bias and weights and  $x$  the input), and defines  $C_{\Delta x_i \Delta a} = w_d \cdot \Delta x_d$  and accordingly  $m_{\Delta x_d \Delta a} = \frac{C_{\Delta x_d \Delta a}}{\Delta x_d}$ . The rescale rule applies to all non-linear transformations  $\sigma(a)$  (e.g., ReLU or sigmoid functions) and defines  $C_{\Delta x \Delta \sigma(a)} = \Delta \sigma(a)$  and accordingly  $m_{\Delta x \Delta \sigma(a)} = \frac{C_{\Delta x \Delta \sigma(a)}}{\Delta x}$ .

**DeepLift SHapley Additive exPlanation (DeepLift SHAP):** DeepLift SHapley Additive exPlanation (DeepLift SHAP) (Lundberg and Lee, 2017) builds on SHAP, a method for computing Shapley values (Shapley, 1952) for a conditional expectation function of the analyzed model. Specifically, SHAP values attribute to each input feature the change in expected model prediction conditioned on the feature of interest. To approximate SHAP values using DeepLift, DeepLift SHAP draws  $N$  (we set  $N = 50$ ) random samples from the data (to approximate the set of other possible feature coalitions) and averages over the DeepLift attributions for each random sample, given a current input, when treating the random sample as a reference input  $b$ .

**Layer-wise relevance propagation (LRP):** Layer-wise relevance propagation (LRP; Bach et al., 2015) is a backward decomposition method that defines relevance  $r$  by the use of relevance messages  $r_{i \leftarrow j}$ , which capture the part of relevance  $r_j$  of model unit  $j$  in layer  $l$  that is redistributed to model unit  $i$  in preceding model layer  $l-1$  during the backward decomposition. To redistribute relevance between layers, several rules have been proposed (Bach et al., 2015, Kohlbrenner et al., 2020, Montavon et al., 2019), which generally follow from  $r_i = \sum_j \frac{a_i \cdot w_{ij}}{\sum_i a_i \cdot w_{ij}} \cdot r_j$ , where  $a$  and  $w$  represent the input and weight of model unit  $i$ . Importantly, LRP conserves relevance between layers, such that:  $\sum_i r_{i \leftarrow j} = r_j$ ;  $r_i = \sum_j r_{i \leftarrow j}$ ;  $\sum_d r_d = \sum_i r_i = \sum_j r_j = f(x)$ . In line with the recommendations by Montavon et al. (2019), we use a composite of relevance redistribution rules,

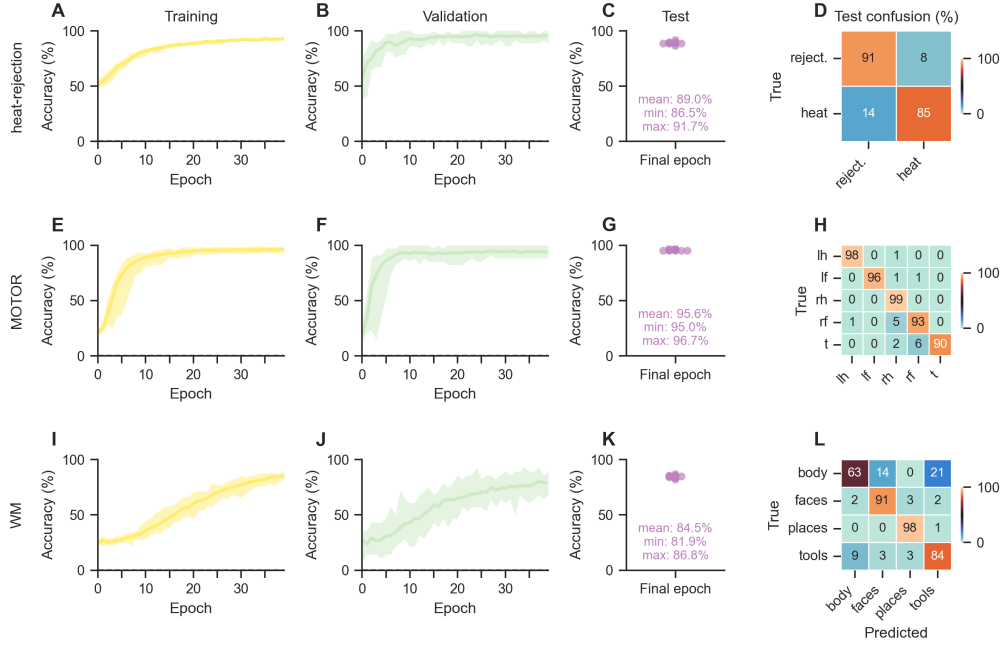


Figure 1: Decoding performance. For each dataset, we trained ten identical variants of each datasets’ model configuration (see section 2.2 of the main text for details on the hyper-parameter optimization) and varied solely the random seed between training runs and the random split into training and validation data (95% and 5% of the full training data). A-B,E-F,I-J: The models performed well in decoding the mental states from the trial-level maps in the training (A,E,I) and validation datasets (B,F,J). Colored lines indicate mean decoding accuracies with shaded areas indicating respective minimum and maximum decoding accuracies across the ten training runs. C-D,G-H,K-L: The final models performed well in decoding the mental states of the left-out test datasets (C,G,K) with generally small confusion rates (D,H,L) (with the exception of the body and tool states of the WM dataset; L). Scatter points indicate the final models’ decoding accuracies in the test data and heatmaps show respective confusion rates averaged over the ten training runs.

namely, the LRP-0 rule ( $r_i = \sum_j \frac{a_i \cdot w_{ij}}{\sum_i a_i \cdot w_{ij}} \cdot r_j$ ) for the dense output layer and the LRP- $\gamma$  rule ( $r_i = \sum_j \frac{a_i \cdot (w_{ij} + \gamma \cdot w_{ij}^+)}{\sum_i a_i \cdot (w_{ij} + \gamma \cdot w_{ij}^+)} \cdot r_j$ , where  $\gamma$  controls the positive contributions to  $r$  (we set  $\gamma = 0.25$ )) for convolution layers.

## 1.5 Code and data availability

All code that we used in this study as well as the trial-level BOLD maps are available at:  
<https://github.com/athms/interpreting-brain-decoding-models>.

## 2 Results

### 2.1 Hyper-parameter optimization

The target of our decoding analyses was to correctly identify the mental state associated with each trial-level BOLD map in the data, namely, "heat" and "rejection" for the heat-rejection dataset, "left foot (lf)", "right foot (rf)", "left hand (lh)", "right hand (rh)", and "tongue (t)" for the



MOTOR dataset, and "body", "faces", "places", and "tools" for the WM dataset (see section 1.1.1).

To determine a configuration of the 3D-CNN architecture for the decoding task of each dataset, we performed a standard hyper-parameter optimization with a grid-search over the number of convolution layers of the model (3, 4 or 5), the number of 3D convolution kernels per convolution layer (4, 8, 16 or 16; Note that we use the same number of kernels for all layers), the size of the individual 3D convolution kernels (3x3x3 or 5x5x5 voxels) as well as the mini-batch size (32 or 64), dropout rate (0.25, 0.5; Srivastava et al., 2014) and learning rate (0.0001, 0.001), resulting in 144 unique model configurations that we tested per dataset.

To evaluate each performance during hyper-parameter optimization, we divided the trial-level BOLD maps of each dataset into separate training and test datasets, by assigning the maps of every 5th individual of a dataset to the test data and the maps of the remaining individuals to the training data. We then evaluated the performance of each model configuration of the grid search in a three-fold cross-validation procedure on the training data, by training each model with stochastic gradient descent (by the use of the ADAM optimizer; Kingma and Ba, 2017) for 40 training epochs per fold (where one epoch is defined as an iteration over the entire training data). To subsequently select a best-performing model configuration for each dataset, we computed the mean decoding error  $\epsilon$  (defined as 1 minus the fraction of correctly decoded trial-level BOLD maps) of each model configuration in the training and validation datasets across the three folds ( $\epsilon^T$  and  $\epsilon^V$  respectively). We then assigned a performance score  $\lambda_i$  to each configuration  $i$ , which we defined as:  $\lambda_i = \epsilon_i^V + |\epsilon_i^V - \epsilon_i^T|$ , thus quantifying how well a model performed in the validation data when also accounting for the difference in model performance between training and validation data (to also minimize overfitting). For each dataset, we defined the best performing model configuration as the configuration with the lowest  $\lambda_i$ .

## 2.2 Models accurately decode mental states

Recent work in DL research has shown that the performance of DL models in a dataset can be strongly dependent on many non-deterministic aspects of the training, such as, random weight initializations and random shuffling of the data during training (Henderson et al., 2018, Lucic et al., 2018, Thomas et al., 2021b). We thus next trained the best-performing model configuration of each dataset (see section 2.1) for ten training runs with the training data, with different random seeds per run and random splits of the data into training/validation datasets. Specifically, for each run, we divided the training dataset into new training and validation datasets by randomly selecting 5% of the trial-level BOLD maps as validation data and using the remaining maps as training data. As before, we trained the models for 40 epochs in each training run (see Fig. 1 A,B,E,F,I,L) and evaluated the decoding performance of the final model in the fixed, left-out test dataset (containing the data of every 5th subject of the full dataset; see Fig. 1 C,G,K and section 2.1). The three model configurations performed well in decoding the mental states of each dataset, with average decoding accuracies (reported as mean [min, max]) in the test dataset of 89.0% [86.5%, 91.7%] (heat-rejection), 95.6% [95%, 96.7%] (MOTOR), and 84.5% [81.9%, 86.8%] (WM). We also computed average test dataset confusion rates (by averaging confusion rates in the test data over the ten training runs per dataset; see Fig. 1 D,H,L) and found that the models generally exhibited very little confusion, with the exception of "tools" and "body" classes of the WM dataset (see Fig. 1 L).

## 2.3 Sensitivity analyses more in line with standard analysis of BOLD data

The foregoing results showed that the models perform well in decoding the mental states of the three datasets. Based on these results, we proceeded to compare the effectiveness of the various

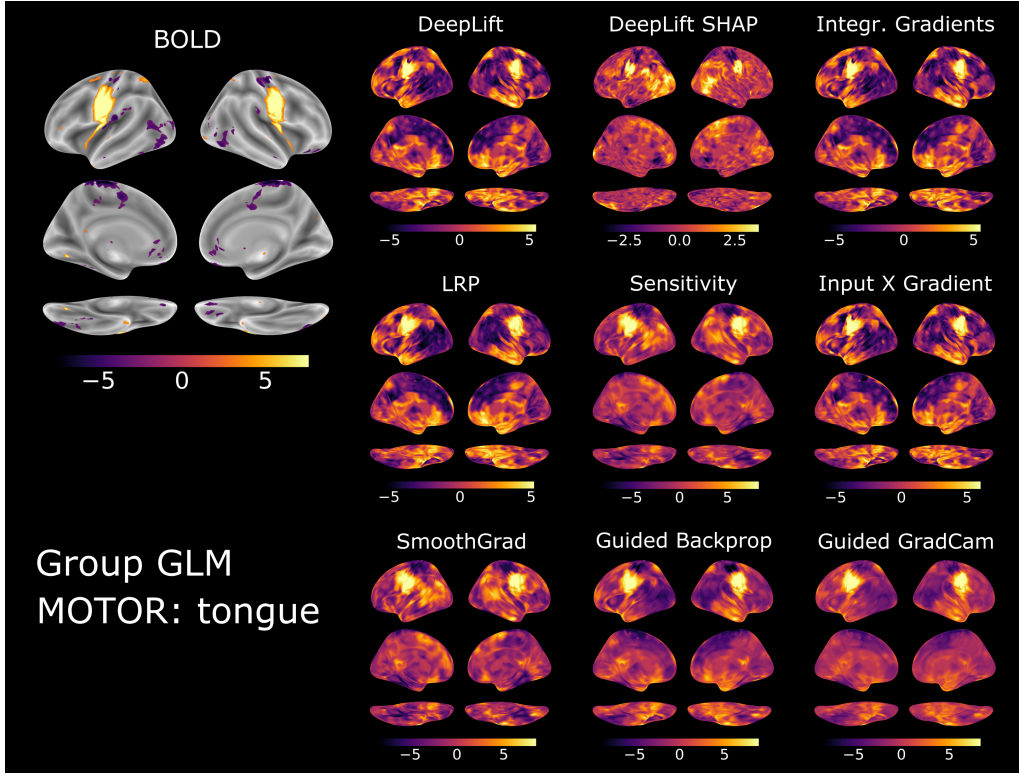


Figure 2: Group-level brain maps for "tongue" movements of the MOTOR dataset. For each dataset, we performed a group-level GLM analysis of its trial-level BOLD maps as well as a group-level GLM analysis of the attributions from each interpretation method for the trial-level BOLD maps in each datasets' test data. Brain maps show the resulting Z-scores of a contrast between the "tongue" state and all other mental states of the MOTOR dataset. All brain maps are projected onto the inflated cortical surface of the FsAverage template (Fischl, 2012). We thresholded the contrast map for the BOLD data at a false positive rate of 0.01.

interpretation techniques (see section 1.4) in providing insight into the models' learned mappings between data and mental states. To this end, we interpreted the decoding decisions of each of the ten trained instances of each datasets' model configuration for each trial-level BOLD map in its respective test dataset. For each interpretation method, this resulted in a dataset of ten attributions maps for each trial-level BOLD map in the test data (one for each trained model instance). Note that we always interpreted the models' decoding decisions for the actual mental state associated with a trial-level BOLD map, as we were interested in understanding the models' learned mappings between this state and the brain activity.

To aggregate the attribution data, we first performed a standard subject-level general linear model (GLM; Friston et al., 1994) analysis of the trial-level attribution maps of each attribution method. This analysis included an indicator vector for each mental state of the dataset, and a set of nuisance regressors, namely, an indicator vector for each of the ten model training runs as well as an indicator vector for each experimental run in the data. We also included a nuisance regressor describing the sum of attribution values for each trial-level map, as the total sum of attribution values can vary highly between decoding decisions (e.g., due to varying decoding certainty of the model). By use of this subject-level regression model, we then contrasted each mental state of a dataset against all other mental states of the dataset, resulting in one subject-level attribution map for each mental state.

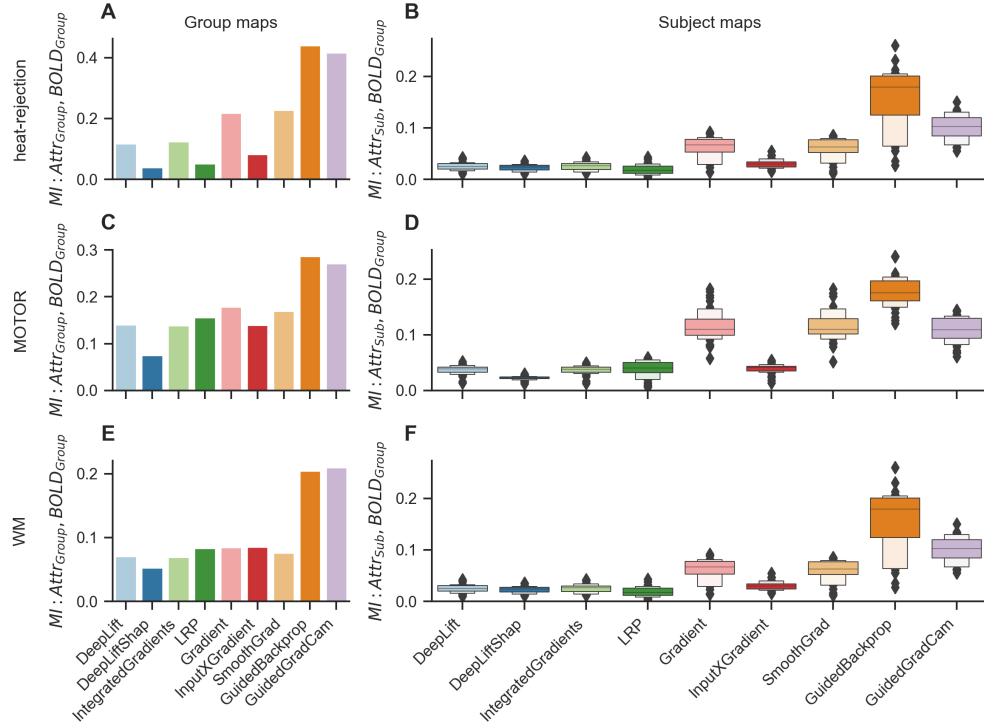


Figure 3: Similarity of attribution maps to group-level BOLD maps. To estimate similarity, we compute the mutual information between the group-level BOLD maps and the group- (A,C,E) and subject-level (B,D,F) attribution maps for each mental state, resulting from an interpretation of each datasets’ models’ decoding decisions for its test data. A,C,E: The group-level maps of Guided Backpropagation and Guided GradCam exhibit overall higher mutual information (i.e., similarity) with the group-level BOLD maps than the group-level maps of the other interpretation methods. Bar heights indicate mean mutual information over the mental states of a dataset. B,D,F: Similarly, the subject-level maps of Guided Backpropagation, Guided GradCam as well as Gradient Analysis and SmoothGrad exhibit higher mutual information with the group-level BOLD maps than the subject-level maps of the other interpretation methods. Letter-value plots (Hofmann et al., 2017) show the distribution of mutual information scores of each interpretation method. Colors indicate interpretation methods.

In a second step of this analysis, we performed a group-level GLM analysis of the individual subject-level attribution maps by the use of the standard two-stage procedure for random-effects group-level analyses as proposed by Holmes and Friston (1998). This analysis included an indicator vector for each contrast type (i.e., mental state) as well as a nuisance indicator vector for each subject. The resulting group-level attribution maps thus correspond to a paired, two-sample t-test over the subject-level attribution maps.

We also repeated this GLM analysis procedure for the trial-level BOLD maps of each dataset (without the nuisance regressors for model training runs and attribution sums), to identify the set of brain regions whose activity we would expect to be associated with each mental state in a standard analysis of the BOLD data.

We provide an example of the resulting group-level BOLD and attribution maps in Fig. 2 for the “tongue” movement state of the MOTOR dataset. For this state, the interpretation methods correctly attributed high attribution values to those voxels in the ventral premotor and primary motor cortex that also showed high activity in the group-level analysis of the BOLD data.

As can be seen, it is generally difficult to discern the quality of the various attributions by visual inspection alone. For this reason, we took a quantitative approach to analyzing how well the results of the individual interpretation methods align with the results of the group-level BOLD analysis, by computing the average mutual information Kraskov et al. (2004) between the group-level attribution maps and the corresponding group-level BOLD maps of the same mental state (see Fig. 3 A,C,E). Note that we chose mutual information as a similarity measure, because the association between the group-level BOLD and attribution maps does not need to be linear. For example, it is possible that a DL model learns to identify a mental state through the activity of voxels that are meaningfully more active in this state as well as the activity of voxels that are meaningfully less active, resulting in an attribution map that assigns high relevance to voxels that exhibit high positive and negative values in a GLM analysis of the BOLD data (see Thomas et al., 2021a).

This analysis revealed that the group-level maps for the attributions of Guided Backpropagation (Springenberg et al., 2015) and Guided GradCam (Selvaraju et al., 2017), two types of sensitivity analysis (see section 1.4), exhibit the overall highest mutual information with the group-level BOLD maps, indicating higher similarity when compared to the group-level maps of the other interpretation methods (see Fig. 3 A,C,E). The group-level attributions of gradient analysis (Simonyan et al., 2014) and SmoothGrad (Smilkov et al., 2017), again two types of sensitivity analyses, also exhibited comparably high similarity with the group-level BOLD maps, achieving consistently high mutual information scores across the three datasets (see Fig. 3 A,C,E).

We were further interested in understanding how well the subject-level attributions of each interpretation align with the group-level BOLD maps and therefore computed the mutual information between each subject-level attribution map and the corresponding group-level BOLD map of the same mental state. Note that we chose to compare the subject-level attribution maps to the group-level BOLD maps, as the interpreted models were trained on the group of subjects contained in each datasets’ training data, thus enabling the models to draw from their knowledge about the group when decoding the trial-level BOLD maps of each individual in the test data. Again, we found that the the subject-level attribution maps of Guided Backpropagation (Springenberg et al., 2015), Guided GradCam (Selvaraju et al., 2017), Gradient analysis (Simonyan et al., 2014), and SmoothGrad (Smilkov et al., 2017) exhibited overall higher mutual information scores than those of the other interpretation methods, indicating overall higher similarity with the group-level BOLD maps.

## 2.4 Backward decompositions and reference-based attributions more faithful

In addition to understanding how well the attributions of each interpretation method align with those of a standard GLM analysis of the trial-level BOLD data, we were interested in understanding how well the methods perform at capturing the decision process of our trained models. To this end, we performed a comparison of the faithfulness (e.g., Samek et al., 2017, 2021) of the attributions resulting from each interpretation method. In general, an attribution map can be viewed as being faithful if it assigns high relevance to those features of the input that are most important for the model’s decoding decision. Accordingly, removing these features from the input should diminish the model’s ability to correctly identify the mental states.

To evaluate the faithfulness of the attributions of an interpretation method, we thus evaluated the decoding accuracy of each trained model in the test data of its dataset when occluding those voxels of the input data that received the highest relevance values by the interpretation method (by setting the voxels’ values to 0). Importantly, we repeated this analysis for different fractions of the data that we occluded, from 0% (indicating no occlusion) to 30% (indicating that the values of all voxels were occluded that received the highest 30% of relevance values) (see Fig. 4 A,C,E). For each attribution method and trained model, we also recorded the occlusion rate at which the

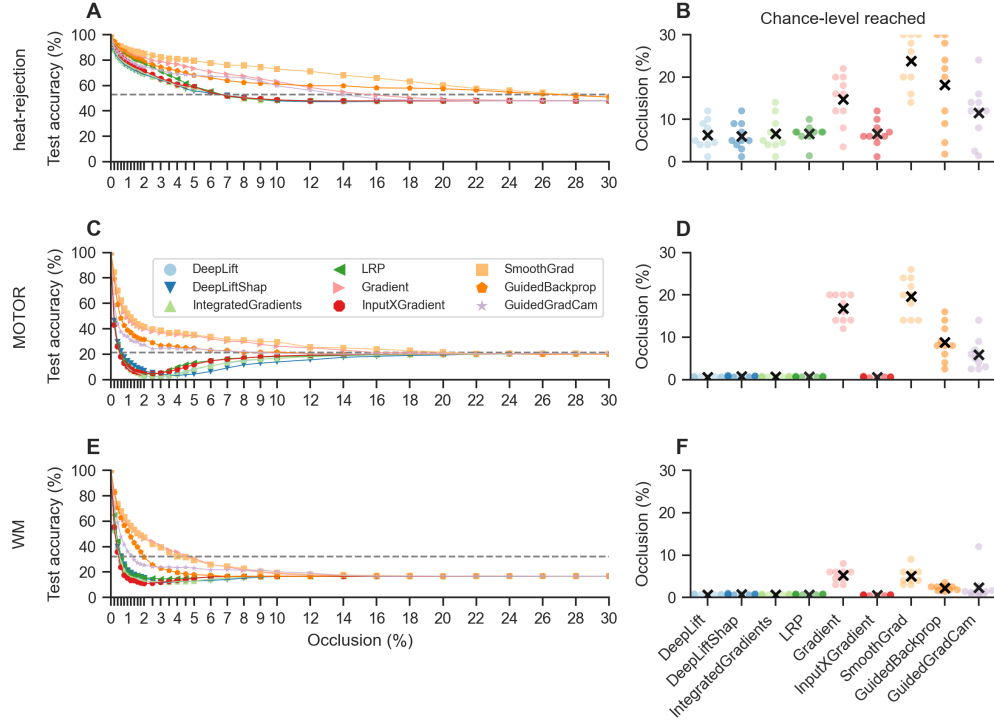


Figure 4: Attribution faithfulness. We estimated attribution faithfulness by repeatedly evaluating the models’ test decoding accuracy when occluding different fractions of the input voxels based on the relevance assigned to them by an interpretation method, such that 0% occlusion indicates that no voxel values were occluded while 30% indicates that the values of all input voxels were occluded that received the highest 30% of relevance values by the interpretation method. For each interpretation method and trained model, we also recorded the occlusion rate at which the models’ test decoding accuracy first drops to chance-level, indicating that all information has been removed from the data that is required by the model to correctly identify the mental states. A,C,E: DeepLift, DeepLift SHAP, LRP, Integrated Gradients, and InputXGradient generally exhibit higher attribution faithfulness than Gradient Analysis, SmoothGrad, Guided Backpropagation, and Guided GradCam, as the models’ test decoding accuracy decreases more rapidly when occluding voxel values based on the highest attributions of these methods. Lines indicate mean test decoding accuracies over the ten training runs of each model configuration. B,D,F: Accordingly, model test decoding accuracies also drop to chance-level at lower occlusion rates for these approaches. Scatter points represent trained models. Black crosses indicate mean occlusion rates over model training runs. Colors indicate interpretation methods.

model’s decoding accuracies first drop to chance level, indicating that all information has been removed from the data that the model requires to accurately identify the associated mental states (see Fig. 4 B,D,F).

Overall, this analysis revealed that the attributions of reference-based attributions and backward decompositions, namely, DeepLift, DeepLift SHAP, Integrated Gradients, and LRP, exhibit higher faithfulness than those of the sensitivity analyses tested in this study, as the models’ decoding decisions dropped to chance level at lower occlusion rates for these methods when compared to the occlusion rates required for the other interpretation methods (with the exception of the InputXGradient (Shrikumar et al., 2017) method whose attribution maps exhibited similar faithfulness to those of the tested backward decompositions and reference-based attributions; see Fig. 4).

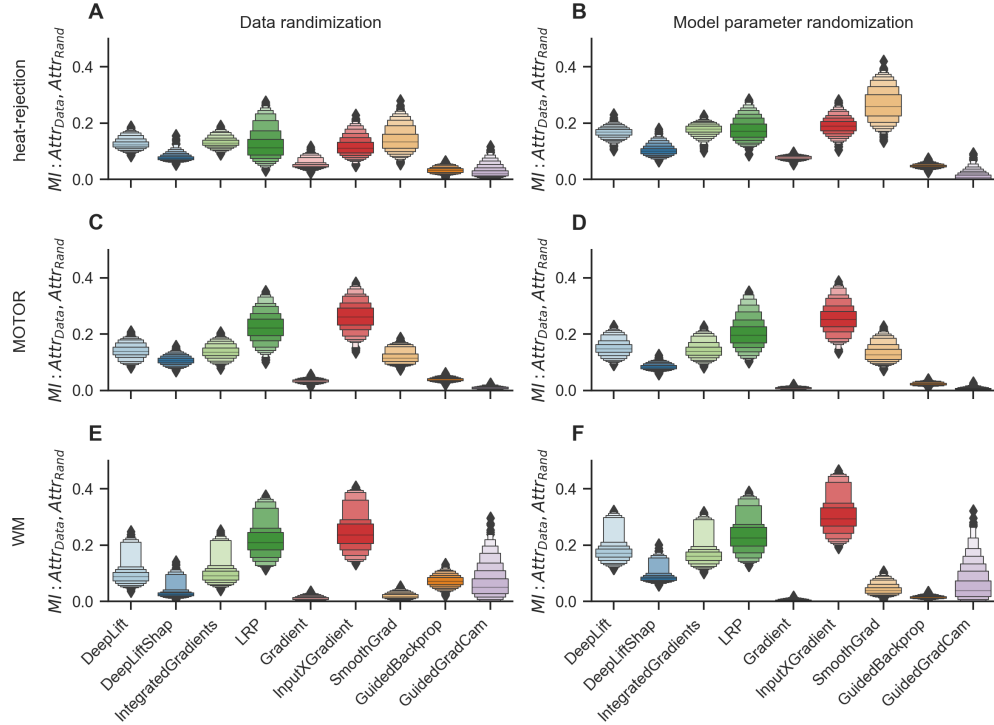


Figure 5: Sanity checks for interpretation methods. We performed two sanity for the attributions of each interpretation method by computing the mutual information between the trial-level attribution maps of the interpretation method for the test decoding decisions of the trained models and the corresponding attributions for a variant of each model configuration that was trained on a version of the original training data with randomized labels (A, C, E) and a variant with randomized model parameters (B, D, F). If the attributions of an interpretation method are dependent on the characteristics of the input data as well as the characteristics of the model, its attributions for the original model and data should be different from its attributions for the model trained on randomized data as well as the model with random parameters (thus resulting in low mutual information). Overall, Gradient Analysis, Guided Backpropagation, Guided GradCam, DeepLift, DeepLift SHAP, and Integrated Gradients perform consistently well in the data randomization (A,C,E) and model randomization (B,D,F) tests, as indicated by the overall low mutual information scores when compared to the other interpretation methods. Letter-value plots (Hofmann et al., 2017) show the distribution of mutual information scores fore each interpretation method in each dataset. Colors indicate interpretation methods.

## 2.5 Sanity checks for interpretation methods

Lastly, we performed two sanity checks for the interpretation methods, as recently proposed by Adebayo et al. (2018) to test the overall scope and quality of their attributions. Specifically, Adebayo et al. (2018) propose two simple tests to ensure that the attributions resulting from an interpretation method are specific to the tested model and data, by testing how much its attributions change when applied to a model with the same architecture but random weights (the model parameter randomization test) and a model trained on a version of the training data with randomly permuted labels (the data randomization test). If the attributions of an interpretation method are dependent on the specific parameters of a model, it should produce attributions that are different when applied to the originally trained models and a model with random weights. If the attributions are similar, however, the interpretation method can be considered insensitive to

the studied model and therefore not well-suited to capture the models’ decision process. Similarly, if the attributions of an interpretation method account for the labeling of the data, then it should produce attributions that are different when applied to a model trained on the original dataset as well as a version of the dataset with randomly shuffled labels. If the attributions are similar, however, the interpretation method can be considered independent of the labeling of the data and therefore not well-suited to understand the model’s learned mapping between these labels and the input data.

In line with the data randomization test, we first trained a variant of each model configuration in each dataset on a version of the original training data with randomly shuffled mental state labels. As DL models are very powerful representation learners, the models were able to correctly decode the randomly shuffled mental state labels in the training data after 2000 training epochs, achieving decoding accuracies of 85.1%, 98.7%, and 98.4% for the heat-rejection, MOTOR, and WM datasets respectively (see Appendix Fig. A1). Note that the models’ decoding accuracies in the respective validation data were still close to chance, indicating that the models memorized the random association between labels and training data (namely, 45.9%, 23.5%, and 25% for the heat-rejection, MOTOR, and WM datasets respectively; see Appendix Fig. A1). Next, we interpreted the decoding decisions of the models trained on randomized data with each interpretation method for the trial-level BOLD maps of their respective test data (comprising every fifth individual of the dataset; see section 2.1). To determine the similarity of the resulting trial-level attribution maps with the trial-level attribution maps for the original model, we again computed their mutual information (see Fig. 5 A,C,E). Overall, this analysis showed Gradient Analysis, Guided Backpropagation, Guided GradCam, DeepLift, DeepLift SHAP, and Integrated Gradients perform well in the data randomization test, as indicated by their consistently low mutual information scores when compared to the other interpretation methods. Their attributions are therefore dependent on the characteristics of the data. The attributions of InputXGradient and LRP, in contrast, are less dependent on the specific labeling of the training data, as indicated by the generally higher mutual information scores.

Similarly, in line with the model parameter randomization test, we also interpreted the mental state decoding decisions of a randomly initialized variant of each datasets’ model configuration for the trial-level BOLD maps of its respective test data. As for the data randomization test, we compared the resulting set of trial-level attribution maps of each interpretation method to their respective trial-level BOLD map counterparts by means of mutual information. Again, this analysis showed that Gradient analysis, Guided Backprop, Guided GradCam, DeepLift, DeepLift SHAP, and Integrated Gradients produce attributions that are dependent on the characteristics of the analyzed model, as indicated by the consistently low mutual information scores. InputX-Gradient and LRP, in contrast, produce attributions that are less consistently dependent on the characteristics of the model, as indicated by the generally higher mutual information scores.

### 3 Discussion

Here, we compared the performance of prominent types of interpretation techniques, namely, sensitivity analyses, backward decompositions, and reference-based attributions (see section 1.4), when applied to the mental state decoding decisions of DL models trained on three fMRI datasets. To evaluate the performance of the tested interpretation methods, we use a diverse set of criteria: First, to test how well their explanations align with the results of a standard analysis of the underlying BOLD data, we measure the similarity of their explanations to the results of a standard GLM analysis of the BOLD data. We find that sensitivity analyses, such as Gradient Analysis and Guided Backpropagation, provide explanations that are more in line with the results of a standard analysis of the BOLD data, when compared to backward decompositions and reference-based attributions. Second, to test how well the techniques perform at capturing a model’s decision process,

we measure the faithfulness of their explanations, by testing whether methods assign the highest attributions scores to those input voxels that are most relevant for the model to identify its set of mental states. We find that backward decompositions and reference-based attributions, such as LRP, DeepLift, DeepLift SHAP, and Integrated Gradients provide explanations that are generally more faithful when compared to sensitivity analyses. Lastly, to test whether the explanations of an interpretation method are sensitive to the analyzed model and data, we perform two sanity checks for interpretation methods (as suggested by Adebayo et al., 2018) and find that the explanations of Gradient Analysis, Guided Backpropagation, DeepLift SHAP, DeepLift, and Integrated Gradients perform consistently well in the sanity checks, providing explanations that are sensitive to the characteristics of the analysed model and input data.

### 3.1 Biological plausibility vs. explanation faithfulness

Our findings indicate a gradient between two key characteristics for the interpretation of mental state decoding decisions: interpretation methods that provide highly faithful explanations, by capturing the decision process of the analyzed model well, also provide explanations that are less in line with the results of a standard analysis of the underlying BOLD data, when compared to interpretation methods with less faithfulness. To make sense of this, it is important to remember that functional neuroimaging data generally exhibit strong spatial correlations, such that individual mental states are often associated with the activity of large clusters of voxels. DL models tasked with identifying these mental states from neuroimaging data will therefore likely view some of this activity as redundant, as the activity of a subset of those voxels suffices to correctly identify the mental states. In these situations, any explanation of an interpretation method with perfect faithfulness will therefore not identify all voxels of the input whose activity is associated with the decoded mental state, but solely the subset of voxels whose activity the model used as evidence for its decoding decision. Accordingly, interpretation methods with high faithfulness, such as backward decompositions and reference-based attributions, do not necessarily produce explanations that align well with the results of a standard GLM analysis of the BOLD data, as they do not necessarily identify all voxels of the input whose activity is in associated with the decoded mental state. In contrast, we found that sensitivity analyses, such as Gradient Analysis and Guided Backpropagation, produce explanations that are less faithful but more in line with the results of a standard GLM analysis of the BOLD data. Sensitivity analyses are less concerned with identifying the specific contribution of each input voxel to a decoding decision and instead focus on identifying how sensitively a model’s decision responds to (i.e., changes with) the activity of each voxel, thereby identifying a broader set of voxels whose activity the model takes into account when decoding the mental state, resulting in explanations that seem biologically more plausible because they identify a set of voxels that is more similar to that identified by standard statistical analyses that seek to identify voxels whose activity is associated with the mental state.

### 3.2 Recommendations for interpretation techniques in mental state decoding

Based on these findings, we make a two-fold recommendation for the application of interpretation techniques in mental state decoding:

If the goal of a mental state decoding analysis is to understand the decision process of the decoding model, by identifying the parts of the input that are most relevant for the model’s decision behavior, we generally recommend the application of backward decompositions or reference-based attributions. In particular, we recommend DeepLift SHAP, DeepLift, and Integrated Gradients, as their explanations have shown overall high faithfulness in our analyses, while also performing well in the two sanity checks, by producing explanations that are specific to the analyzed model and data. Note that DeepLift and Integrated Gradients are generally considered closely related



Ancona et al. (2018), while DeepLift (with the Rescale rule used in this work; see section 1.4) is generally faster to compute.

In contrast, if the goal of a mental state decoding analysis is to understand the association between the BOLD data and studied mental states, we generally recommend the application of sensitivity analyses, as these have shown to produce explanations with relatively high similarity to the results of a standard GLM analysis of the BOLD data, when compared to reference-based attributions or backward decompositions. Particularly, we recommend Guided Backpropagation as its explanations exhibit the highest similarity to the results of a standard GLM analysis of the BOLD data in our analyses, while also performing well in the two sanity checks. As an alternative, for models that do not include ReLU activation functions, we recommend the application of standard Gradient Analysis, as its explanations also exhibit relatively high similarity to the results of a standard GLM analysis of the BOLD data, especially on the level of individual subjects, while also performing well in the two sanity checks.

### 3.3 Caution in the application of complex models

Lastly, we would like to advocate for caution in any interpretation of mental state decoding decisions of DL models. DL models have an unmatched ability to learn from and represent complex data. Accordingly, their learned mappings between input data and decoding decisions can be highly-complex and counterintuitive. For example, recent empirical work has shown that DL methods trained in mental state decoding analyses can identify individual mental states through voxels that exhibit meaningfully stronger activity in these states as well as voxels with meaningfully reduced activity in these states, leading to explanations that assign high attribution scores to voxels that receive both positive and negative weights in a standard GLM contrast analysis of the same BOLD data (Thomas et al., 2021a). It is thus essential to always interpret any explanations of an interpretation method in the light of the results of standard analyses of the same BOLD data (e.g., with linear models Friston et al., 1994, Grosenick et al., 2013, Kriegeskorte et al., 2006) as well as related empirical findings (e.g., as provided by NeuroSynth; Yarkoni et al., 2011), to understand how a model’s weighting of the input in its decoding decision relates to the characteristics of the input data.

Similarly, a wealth of recent empirical findings in machine learning research have demonstrated that DL models are prone to learning simple shortcuts (or confounds) from their training data, which do not necessarily generalize well to new datasets (for a detailed discussion, see Geirhos et al., 2020). A prominent example is a study that trained DL models to identify pneumonia from chest X-rays (Zech et al., 2018). While the models performed well in the training data, comprising X-rays from few hospitals, their performance meaningfully decreased for X-rays from new hospitals. By applying interpretation methods to the classification decisions of the trained models, the authors were able to show that the models learned to accurately identify the hospital system that was used to acquire an X-ray, in combination with the specific department, allowing them to make accurate predictions on aggregate in the training data by simply learning the overall prevalence rates of these departments. Similar examples are imaginable in functional neuroimaging, as recently suggested by Chyzhyk et al. (2022), who state that biomarker models for specific disease conditions may learn to distinguish patients from controls by their generally increased head motion.

For these reasons, we echo a recent call of machine learning researchers to always consider whether the application of complex models (such as DL models) is necessary to answer the research question at hand, or whether the application of simpler models, with better interpretability, could suffice (Rudin, 2019) (especially in high-stakes decision situations, such as the development of biomarker disease models). While we do believe that DL models hold a high promise for the field of mental state decoding, e.g., in their ability to learn from large-scale neuroimaging datasets (Schulz et al., 2022), we also believe that many common mental state decoding analyses, which focus on few mental states in tens to a hundred of individuals, can be well-addressed with simpler

decoding models with better interpretability (e.g., Grosenick et al., 2013, Hoyos-Idrobo et al., 2018, Kriegeskorte et al., 2006, Michel et al., 2011, Schulz et al., 2020).

Lastly, we would like to emphasize that any interpretation method represents its own model, with specific characteristics and assumptions, that is applied to a DL model, which by itself is not interpretable. Each interpretation method thus has its own strengths and weaknesses in different contexts and it is important to make an informed choice on when to apply which of these methods. We hope that with this work we can provide insights for neuroimaging researchers into the characteristics of several prominent interpretation methods in mental state decoding, enabling them to make an informed choice in situations where insights into the mental state decoding decisions of DL models are needed.

**Acknowledgments.** Armin W. Thomas is supported by Stanford Data Science through the Ram and Vijay Shriram Data Science Fellowship. Russell A. Poldrack is supported by the National Science Foundation under Grant No. OAC-1760950. Christopher Ré gratefully acknowledges the support of NIH under No. U54EB020405 (Mobilize), NSF under Nos. CCF1763315 (Beyond Sparsity), CCF1563078 (Volume to Velocity), and 1937301 (RTML); ONR under No. N000141712266 (Unifying Weak Supervision); the Moore Foundation, NXP, Xilinx, LETI-CEA, Intel, IBM, Microsoft, NEC, Toshiba, TSMC, ARM, Hitachi, BASF, Accenture, Ericsson, Qualcomm, Analog Devices, the Okawa Foundation, American Family Insurance, Google Cloud, Salesforce, Total, the HAI-AWS Cloud Credits for Research program, Stanford Data Science, and members of the Stanford DAWN project: Facebook, Google, and VMWare. The Mobilize Center is a Biomedical Technology Resource Center, funded by the NIH National Institute of Biomedical Imaging and Bioengineering through Grant P41EB027060. The U.S. Government is authorized to reproduce and distribute reprints for Governmental purposes notwithstanding any copyright notation thereon. Any opinions, findings, and conclusions or recommendations expressed in this material are those of the authors and do not necessarily reflect the views, policies, or endorsements, either expressed or implied, of NIH, ONR, or the U.S. Government.

FMRI data for the MOTOR and WM datasets were provided by the Human Connectome Project (HCP S1200 release), WU Minn Consortium (Principal Investigators: David Van Essen and Kamil Ugurbil; 1U54MH091657) funded by the 16 NIH Institutes and Centers that support the NIH Blueprint for Neuroscience Research; and by the McDonnell Center for Systems Neuroscience at Washington University. FMRI data for the heat-rejection dataset were publicly shared in a preprocessed format by Kohoutová et al. (2020).

## References

- Abraham, A., Pedregosa, F., Eickenberg, M., Gervais, P., Mueller, A., Kossaifi, J., Gramfort, A., Thirion, B., and Varoquaux, G. (2014a). Machine learning for neuroimaging with scikit-learn. *Frontiers in Neuroinformatics*, 8.
- Abraham, A., Pedregosa, F., Eickenberg, M., Gervais, P., Mueller, A., Kossaifi, J., Gramfort, A., Thirion, B., and Varoquaux, G. (2014b). Machine learning for neuroimaging with scikit-learn. *Frontiers in Neuroinformatics*, 8.
- Abrol, A., Fu, Z., Salman, M., Silva, R., Du, Y., Plis, S., and Calhoun, V. (2021). Deep learning encodes robust discriminative neuroimaging representations to outperform standard machine learning. *Nature communications*, 12(1):1–17. Publisher: Nature Publishing Group.
- Adebayo, J., Gilmer, J., Muelly, M., Goodfellow, I., Hardt, M., and Kim, B. (2018). Sanity checks for saliency maps. In *Proceedings of the 32nd International Conference on Neural Information Processing Systems*, NIPS’18, pages 9525–9536, Red Hook, NY, USA. Curran Associates Inc.

- Agarap, A. F. (2019). Deep Learning using Rectified Linear Units (ReLU). *arXiv:1803.08375 [cs, stat]*. arXiv: 1803.08375.
- Ancona, M., Ceolini, E., Öztireli, C., and Gross, M. (2018). Towards better understanding of gradient-based attribution methods for Deep Neural Networks. *6th International Conference on Learning Representations (ICLR)*, (1711.06104):0–0. Number: 1711.06104 Place: Ithaca, NY, USA Publisher: Arxiv - Computer Science.
- Avants, B., Epstein, C., Grossman, M., and Gee, J. (2008). Symmetric diffeomorphic image registration with cross-correlation: Evaluating automated labeling of elderly and neurodegenerative brain. *Medical Image Analysis*, 12(1):26–41.
- Bach, S., Binder, A., Montavon, G., Klauschen, F., Müller, K.-R., and Samek, W. (2015). On Pixel-Wise Explanations for Non-Linear Classifier Decisions by Layer-Wise Relevance Propagation. *PLOS ONE*, 10(7):e0130140.
- Behzadi, Y., Restom, K., Liau, J., and Liu, T. T. (2007). A component based noise correction method (CompCor) for BOLD and perfusion based fmri. *NeuroImage*, 37(1):90–101.
- Chyzhyk, D., Varoquaux, G., Milham, M., and Thirion, B. (2022). How to remove or control confounds in predictive models, with applications to brain biomarkers. *GigaScience*, 11:giac014.
- Dadi, K., Rahim, M., Abraham, A., Chyzhyk, D., Milham, M., Thirion, B., and Varoquaux, G. (2019). Benchmarking functional connectome-based predictive models for resting-state fMRI. *NeuroImage*, 192:115–134.
- Ding, S. and Koehn, P. (2021). Evaluating Saliency Methods for Neural Language Models. Technical Report arXiv:2104.05824, arXiv. arXiv:2104.05824 [cs] type: article.
- Doshi-Velez, F. and Kim, B. (2017). Towards A Rigorous Science of Interpretable Machine Learning. *arXiv:1702.08608 [cs, stat]*. arXiv: 1702.08608.
- Esteban, O., Blair, R., Markiewicz, C. J., Berleant, S. L., Moodie, C., Ma, F., Isik, A. I., Erramuzpe, A., Kent, James D. andGoncalves, M., DuPre, E., Sitek, K. R., Gomez, D. E. P., Lurie, D. J., Ye, Z., Poldrack, R. A., and Gorgolewski, K. J. (2018a). fmriprep. *Software*.
- Esteban, O., Markiewicz, C., Blair, R. W., Moodie, C., Isik, A. I., Erramuzpe Aliaga, A., Kent, J., Goncalves, M., DuPre, E., Snyder, M., Oya, H., Ghosh, S., Wright, J., Durnez, J., Poldrack, R., and Gorgolewski, K. J. (2018b). fMRIPrep: a robust preprocessing pipeline for functional MRI. *Nature Methods*.
- Esteban, O., Markiewicz, C. J., Blair, R. W., Moodie, C. A., Isik, A. I., Erramuzpe, A., Kent, J. D., Goncalves, M., DuPre, E., Snyder, M., Oya, H., Ghosh, S. S., Wright, J., Durnez, J., Poldrack, R. A., and Gorgolewski, K. J. (2019). fMRIPrep: a robust preprocessing pipeline for functional MRI. *Nature Methods*, 16(1):111–116.
- Evans, A., Janke, A., Collins, D., and Baillet, S. (2012). Brain templates and atlases. *NeuroImage*, 62(2):911–922.
- Fischl, B. (2012). FreeSurfer. *NeuroImage*, 62(2):774–781.
- Fonov, V., Evans, A., McKinstry, R., Alml, C., and Collins, D. (2009). Unbiased nonlinear average age-appropriate brain templates from birth to adulthood. *NeuroImage*, 47, Supplement 1:S102.
- Friston, K. J., Holmes, A. P., Worsley, K. J., Poline, J.-P., Frith, C. D., and Frackowiak, R. S. J. (1994). Statistical parametric maps in functional imaging: A general linear approach. *Human Brain Mapping*, 2(4):189–210.

- Geirhos, R., Jacobsen, J.-H., Michaelis, C., Zemel, R., Brendel, W., Bethge, M., and Wichmann, F. A. (2020). Shortcut learning in deep neural networks. *Nature Machine Intelligence*, 2(11):665–673.
- Gilpin, L. H., Bau, D., Yuan, B. Z., Bajwa, A., Specter, M., and Kagal, L. (2018). Explaining Explanations: An Overview of Interpretability of Machine Learning. In *2018 IEEE 5th International Conference on Data Science and Advanced Analytics (DSAA)*, pages 80–89.
- Goodfellow, I., Bengio, Y., and Courville, A. (2016). *Deep Learning*. MIT Press.
- Gorgolewski, K., Burns, C. D., Madison, C., Clark, D., Halchenko, Y. O., Waskom, M. L., and Ghosh, S. (2011). Nipype: a flexible, lightweight and extensible neuroimaging data processing framework in python. *Frontiers in Neuroinformatics*, 5:13.
- Gorgolewski, K. J., Esteban, O., Markiewicz, C. J., Ziegler, E., Ellis, D. G., Notter, M. P., Jarecka, D., Johnson, H., Burns, C., Manhães-Savio, A., Hamalainen, C., Yvernault, B., Salo, T., Jordan, K., Goncalves, M., Waskom, M., Clark, D., Wong, J., Loney, F., Modat, M., Dewey, B. E., Madison, C., Visconti di Oleggio Castello, M., Clark, M. G., Dayan, M., Clark, D., Keshavan, A., Pinsard, B., Gramfort, A., Berleant, S., Nielson, D. M., Bougacha, S., Varoquaux, G., Cipollini, B., Markello, R., Rokem, A., Moloney, B., Halchenko, Y. O., Wassermann, D., Hanke, M., Horea, C., Kaczmarzyk, J., de Hollander, G., DuPre, E., Gillman, A., Mordom, D., Buchanan, C., Tungaraza, R., Pauli, W. M., Iqbal, S., Sikka, S., Mancini, M., Schwartz, Y., Malone, I. B., Dubois, M., Frohlich, C., Welch, D., Forbes, J., Kent, J., Watanabe, A., Cumba, C., Huntenburg, J. M., Kastman, E., Nichols, B. N., Eshaghi, A., Ginsburg, D., Schaefer, A., Acland, B., Giavasis, S., Kleesiek, J., Erickson, D., Küttner, R., Haselgrove, C., Correa, C., Ghayoor, A., Liem, F., Millman, J., Haehn, D., Lai, J., Zhou, D., Blair, R., Glatard, T., Renfro, M., Liu, S., Kahn, A. E., Pérez-García, F., Triplett, W., Lampe, L., Stadler, J., Kong, X.-Z., Hallquist, M., Chetverikov, A., Salvatore, J., Park, A., Poldrack, R., Craddock, R. C., Inati, S., Hinds, O., Cooper, G., Perkins, L. N., Marina, A., Mattfeld, A., Noel, M., Snoek, L., Matsubara, K., Cheung, B., Rothmei, S., Urchs, S., Durnez, J., Mertz, F., Geisler, D., Floren, A., Gerhard, S., Sharp, P., Molina-Romero, M., Weinstein, A., Broderick, W., Saase, V., Andberg, S. K., Harms, R., Schlamp, K., Arias, J., Papadopoulos Orfanos, D., Tarbert, C., Tambini, A., De La Vega, A., Nickson, T., Brett, M., Falkiewicz, M., Podranski, K., Linkersdörfer, J., Flandin, G., Ort, E., Shachnev, D., McNamee, D., Davison, A., Varada, J., Schwabacher, I., Pellman, J., Perez-Guevara, M., Khanuja, R., Pannetier, N., McDermottroe, C., and Ghosh, S. (2018). Nipype. *Software*.
- Greve, D. N. and Fischl, B. (2009). Accurate and robust brain image alignment using boundary-based registration. *NeuroImage*, 48(1):63–72.
- Grosenick, L., Klingenberg, B., Katovich, K., Knutson, B., and Taylor, J. E. (2013). Interpretable whole-brain prediction analysis with GraphNet. *NeuroImage*, 72:304–321.
- Haynes, J.-D. and Rees, G. (2006). Decoding mental states from brain activity in humans. *Nature Reviews Neuroscience*, 7(7):523–534. Number: 7 Publisher: Nature Publishing Group.
- Henderson, P., Islam, R., Bachman, P., Pineau, J., Precup, D., and Meger, D. (2018). Deep Reinforcement Learning That Matters. In *Proceedings of the AAAI Conference on Artificial Intelligence*, volume 32.
- Hofmann, H., Wickham, H., and Kafadar, K. (2017). Letter-Value Plots: Boxplots for Large Data. *Journal of Computational and Graphical Statistics*, 26(3):469–477. Publisher: Taylor & Francis eprint: <https://doi.org/10.1080/10618600.2017.1305277>.

- Holmes, A. P. and Friston, K. J. (1998). Generalisability, Random Effects & Population Inference. *NeuroImage*, 7(4, Part 2):S754.
- Hoyos-Idrobo, A., Varoquaux, G., Schwartz, Y., and Thirion, B. (2018). FReM – Scalable and stable decoding with fast regularized ensemble of models. *NeuroImage*, 180:160–172.
- Jacovi, A. and Goldberg, Y. (2020). Towards Faithfully Interpretable NLP Systems: How Should We Define and Evaluate Faithfulness? In *Proceedings of the 58th Annual Meeting of the Association for Computational Linguistics*, pages 4198–4205, Online. Association for Computational Linguistics.
- Jain, S. and Wallace, B. C. (2019). Attention is not Explanation. *arXiv:1902.10186 [cs]*. arXiv: 1902.10186.
- Jenkinson, M., Bannister, P., Brady, M., and Smith, S. (2002). Improved optimization for the robust and accurate linear registration and motion correction of brain images. *NeuroImage*, 17(2):825–841.
- Jenkinson, M. and Smith, S. (2001). A global optimisation method for robust affine registration of brain images. *Medical Image Analysis*, 5(2):143–156.
- Kindermans, P.-J., Hooker, S., Adebayo, J., Alber, M., Schütt, K. T., Dähne, S., Erhan, D., and Kim, B. (2019). The (Un)reliability of Saliency Methods. In Samek, W., Montavon, G., Vedaldi, A., Hansen, L. K., and Müller, K.-R., editors, *Explainable AI: Interpreting, Explaining and Visualizing Deep Learning*, Lecture Notes in Computer Science, pages 267–280. Springer International Publishing, Cham.
- Kingma, D. P. and Ba, J. (2017). Adam: A Method for Stochastic Optimization. *arXiv:1412.6980 [cs]*. arXiv: 1412.6980.
- Kohlbrenner, M., Bauer, A., Nakajima, S., Binder, A., Samek, W., and Lapuschkin, S. (2020). Towards Best Practice in Explaining Neural Network Decisions with LRP. In *2020 International Joint Conference on Neural Networks (IJCNN)*, pages 1–7.
- Kohoutová, L., Heo, J., Cha, S., Lee, S., Moon, T., Wager, T. D., and Woo, C.-W. (2020). Toward a unified framework for interpreting machine-learning models in neuroimaging. *Nature Protocols*, 15(4):1399–1435. Number: 4 Publisher: Nature Publishing Group.
- Kraskov, A., Stögbauer, H., and Grassberger, P. (2004). Estimating mutual information. *Physical Review E*, 69(6):066138. Publisher: American Physical Society.
- Kriegeskorte, N., Goebel, R., and Bandettini, P. (2006). Information-based functional brain mapping. *Proceedings of the National Academy of Sciences*, 103(10):3863–3868.
- Lanczos, C. (1964). Evaluation of noisy data. *Journal of the Society for Industrial and Applied Mathematics Series B Numerical Analysis*, 1(1):76–85.
- LeCun, Y., Bengio, Y., and Hinton, G. (2015). Deep learning. *Nature*, 521(7553):436–444.
- LeCun, Y., Bengio, Y., and Laboratoires, T. B. (1998). Convolutional Networks for Images, Speech, and Time-Series. page 15.
- Linardatos, P., Papastefanopoulos, V., and Kotsiantis, S. (2021). Explainable AI: A Review of Machine Learning Interpretability Methods. *Entropy*, 23(1):18. Number: 1 Publisher: Multidisciplinary Digital Publishing Institute.

- Lucic, M., Kurach, K., Michalski, M., Gelly, S., and Bousquet, O. (2018). Are GANs Created Equal? A Large-Scale Study. In *Advances in Neural Information Processing Systems*, volume 31.
- Lundberg, S. M. and Lee, S.-I. (2017). A Unified Approach to Interpreting Model Predictions. In Guyon, I., Luxburg, U. V., Bengio, S., Wallach, H., Fergus, R., Vishwanathan, S., and Garnett, R., editors, *Advances in Neural Information Processing Systems*, volume 30. Curran Associates, Inc.
- Mensch, A., Mairal, J., Thirion, B., and Varoquaux, G. (2021). Extracting representations of cognition across neuroimaging studies improves brain decoding. *PLOS Computational Biology*, 17(5):e1008795.
- Michel, V., Gramfort, A., Varoquaux, G., Eger, E., and Thirion, B. (2011). Total Variation Regularization for fMRI-Based Prediction of Behavior. *IEEE Transactions on Medical Imaging*, 30(7):1328–1340. Conference Name: IEEE Transactions on Medical Imaging.
- Montavon, G., Binder, A., Lapuschkin, S., Samek, W., and Müller, K.-R. (2019). Layer-Wise Relevance Propagation: An Overview. In Samek, W., Montavon, G., Vedaldi, A., Hansen, L. K., and Müller, K.-R., editors, *Explainable AI: Interpreting, Explaining and Visualizing Deep Learning*, Lecture Notes in Computer Science, pages 193–209. Springer International Publishing, Cham.
- Montavon, G., Lapuschkin, S., Binder, A., Samek, W., and Müller, K.-R. (2017). Explaining nonlinear classification decisions with deep Taylor decomposition. *Pattern Recognition*, 65:211–222.
- Plis, S. M., Hjelm, D. R., Salakhutdinov, R., Allen, E. A., Bockholt, H. J., Long, J. D., Johnson, H. J., Paulsen, J. S., Turner, J. A., and Calhoun, V. D. (2014). Deep learning for neuroimaging: a validation study. *Frontiers in Neuroscience*, 8. Publisher: Frontiers.
- Power, J. D., Mitra, A., Laumann, T. O., Snyder, A. Z., Schlaggar, B. L., and Petersen, S. E. (2014). Methods to detect, characterize, and remove motion artifact in resting state fmri. *NeuroImage*, 84(Supplement C):320–341.
- Pruim, R. H. R., Mennes, M., van Rooij, D., Llera, A., Buitelaar, J. K., and Beckmann, C. F. (2015). Ica-AROMA: A robust ICA-based strategy for removing motion artifacts from fmri data. *NeuroImage*, 112(Supplement C):267–277.
- Rudin, C. (2019). Stop explaining black box machine learning models for high stakes decisions and use interpretable models instead. *Nature Machine Intelligence*, 1(5):206–215. Number: 5 Publisher: Nature Publishing Group.
- Samek, W., Binder, A., Montavon, G., Lapuschkin, S., and Müller, K.-R. (2017). Evaluating the Visualization of What a Deep Neural Network Has Learned. *IEEE Transactions on Neural Networks and Learning Systems*, 28(11):2660–2673. Conference Name: IEEE Transactions on Neural Networks and Learning Systems.
- Samek, W., Montavon, G., Lapuschkin, S., Anders, C. J., and Müller, K.-R. (2021). Explaining Deep Neural Networks and Beyond: A Review of Methods and Applications. *Proceedings of the IEEE*, 109(3):247–278.
- Satterthwaite, T. D., Elliott, M. A., Gerraty, R. T., Ruparel, K., Loughead, J., Calkins, M. E., Eickhoff, S. B., Hakonarson, H., Gur, R. C., Gur, R. E., and Wolf, D. H. (2013). An improved framework for confound regression and filtering for control of motion artifact in the preprocessing of resting-state functional connectivity data. *NeuroImage*, 64(1):240–256.

- Schulz, M.-A., Bzdok, D., Haufe, S., Haynes, J.-D., and Ritter, K. (2022). Performance reserves in brain-imaging-based phenotype prediction. preprint, Neuroscience.
- Schulz, M.-A., Yeo, B. T. T., Vogelstein, J. T., Mourao-Miranada, J., Kather, J. N., Kording, K., Richards, B., and Bzdok, D. (2020). Different scaling of linear models and deep learning in UK Biobank brain images versus machine-learning datasets. *Nature Communications*, 11(1):4238.
- Selvaraju, R. R., Cogswell, M., Das, A., Vedantam, R., Parikh, D., and Batra, D. (2017). Grad-CAM: Visual Explanations from Deep Networks via Gradient-Based Localization. In *2017 IEEE International Conference on Computer Vision (ICCV)*, pages 618–626. ISSN: 2380-7504.
- Shapley, L. S. (1952). A Value for N-Person Games. Technical report, RAND Corporation.
- Shrikumar, A., Greenside, P., and Kundaje, A. (2017). Learning Important Features Through Propagating Activation Differences. In *International Conference on Machine Learning*, pages 3145–3153. PMLR. ISSN: 2640-3498.
- Simonyan, K., Vedaldi, A., and Zisserman, A. (2014). Deep Inside Convolutional Networks: Visualising Image Classification Models and Saliency Maps. *arXiv:1312.6034 [cs]*. arXiv: 1312.6034.
- Smilkov, D., Thorat, N., Kim, B., Viégas, F., and Wattenberg, M. (2017). SmoothGrad: removing noise by adding noise. *arXiv:1706.03825 [cs, stat]*. arXiv: 1706.03825.
- Springenberg, J. T., Dosovitskiy, A., Brox, T., and Riedmiller, M. (2015). Striving for Simplicity: The All Convolutional Net. *arXiv:1412.6806 [cs]*. arXiv: 1412.6806.
- Srivastava, N., Hinton, G., Krizhevsky, A., Sutskever, I., and Salakhutdinov, R. (2014). Dropout: A Simple Way to Prevent Neural Networks from Overfitting. *Journal of Machine Learning Research*, 15(56):1929–1958.
- Sundararajan, M., Taly, A., and Yan, Q. (2017). Axiomatic attribution for deep networks. In *Proceedings of the 34th International Conference on Machine Learning - Volume 70, ICML’17*, pages 3319–3328, Sydney, NSW, Australia. JMLR.org.
- Thomas, A. W., Heekeren, H. R., Müller, K.-R., and Samek, W. (2019). Analyzing Neuroimaging Data Through Recurrent Deep Learning Models. *Frontiers in Neuroscience*, 13:1321.
- Thomas, A. W., Lindenberger, U., Samek, W., and Müller, K.-R. (2021a). Evaluating deep transfer learning for whole-brain cognitive decoding. *arXiv:2111.01562 [cs, q-bio]*. arXiv: 2111.01562.
- Thomas, A. W., Ré, C., and Poldrack, R. A. (2021b). Challenges for cognitive decoding using deep learning methods. *arXiv:2108.06896 [cs, stat]*. arXiv: 2108.06896.
- Tustison, N. J., Avants, B. B., Cook, P. A., Zheng, Y., Egan, A., Yushkevich, P. A., and Gee, J. C. (2010). N4itk: Improved n3 bias correction. *IEEE Transactions on Medical Imaging*, 29(6):1310–1320.
- Uğurbil, K., Xu, J., Auerbach, E. J., Moeller, S., Vu, A. T., Duarte-Carvajalino, J. M., Lenglet, C., Wu, X., Schmitter, S., Van de Moortele, P. F., Strupp, J., Sapiro, G., De Martino, F., Wang, D., Harel, N., Garwood, M., Chen, L., Feinberg, D. A., Smith, S. M., Miller, K. L., Sotiropoulos, S. N., Jbabdi, S., Andersson, J. L. R., Behrens, T. E. J., Glasser, M. F., Van Essen, D. C., and Yacoub, E. (2013). Pushing spatial and temporal resolution for functional and diffusion MRI in the Human Connectome Project. *NeuroImage*, 80:80–104.
- Van Essen, D. C., Smith, S. M., Barch, D. M., Behrens, T. E. J., Yacoub, E., and Ugurbil, K. (2013). The WU-Minn Human Connectome Project: An overview. *NeuroImage*, 80:62–79.

- VanRullen, R. and Reddy, L. (2019). Reconstructing faces from fMRI patterns using deep generative neural networks. *Communications Biology*, 2(1):1–10. Number: 1 Publisher: Nature Publishing Group.
- Wang, X., Liang, X., Jiang, Z., Nguchu, B. A., Zhou, Y., Wang, Y., Wang, H., Li, Y., Zhu, Y., Wu, F., Gao, J.-H., and Qiu, B. (2020). Decoding and mapping task states of the human brain via deep learning. *Human Brain Mapping*, 41(6):1505–1519.
- Woo, C.-W., Koban, L., Kross, E., Lindquist, M. A., Banich, M. T., Ruzic, L., Andrews-Hanna, J. R., and Wager, T. D. (2014). Separate neural representations for physical pain and social rejection. *Nature Communications*, 5(1):5380. Number: 1 Publisher: Nature Publishing Group.
- Yarkoni, T., Poldrack, R. A., Nichols, T. E., Van Essen, D. C., and Wager, T. D. (2011). Large-scale automated synthesis of human functional neuroimaging data. *Nature Methods*, 8(8):665–670. Number: 8 Publisher: Nature Publishing Group.
- Zech, J. R., Badgeley, M. A., Liu, M., Costa, A. B., Titano, J. J., and Oermann, E. K. (2018). Variable generalization performance of a deep learning model to detect pneumonia in chest radiographs: A cross-sectional study. *PLOS Medicine*, 15(11):e1002683.
- Zhang, Y., Brady, M., and Smith, S. (2001). Segmentation of brain MR images through a hidden markov random field model and the expectation-maximization algorithm. *IEEE Transactions on Medical Imaging*, 20(1):45–57.
- Zhang, Y., Tetrel, L., Thirion, B., and Bellec, P. (2021). Functional annotation of human cognitive states using deep graph convolution. *NeuroImage*, 231:117847.
- Zurada, J., Malinowski, A., and Cloete, I. (1994). Sensitivity analysis for minimization of input data dimension for feedforward neural network. In *Proceedings of IEEE International Symposium on Circuits and Systems - ISCAS '94*, volume 6, pages 447–450 vol.6.



## A Methods

### A.1 Data

#### A.1.1 Fmriprep details

Results included in this manuscript come from preprocessing performed using *fMRIPrep* 20.2.3 (Esteban et al. (2018b); Esteban et al. (2018a); RRID:SCR\_016216), which is based on *Nipype* 1.6.1 (Gorgolewski et al. (2011); Gorgolewski et al. (2018); RRID:SCR\_002502).

**Anatomical data preprocessing** The T1-weighted (T1w) images were corrected for intensity non-uniformity (INU) with `N4BiasFieldCorrection` (Tustison et al., 2010), distributed with ANTs 2.3.3 (Avants et al., 2008, RRID:SCR\_004757), and used as T1w-reference throughout the workflow. The T1w-reference was then skull-stripped with a *Nipype* implementation of the `antsBrainExtraction.sh` workflow (from ANTs), using OASIS30ANTs as target template. Brain tissue segmentation of cerebrospinal fluid (CSF), white-matter (WM) and gray-matter (GM) was performed on the brain-extracted T1w using `fast` (FSL 5.0.9, RRID:SCR\_002823, Zhang et al., 2001). Volume-based spatial normalization to two standard spaces (MNI152NLin2009cAsym, MNI152NLin6Asym) was performed through nonlinear registration with `antsRegistration` (ANTs 2.3.3), using brain-extracted versions of both T1w reference and the T1w template. The following templates were selected for spatial normalization: *ICBM 152 Nonlinear Asymmetrical template version 2009c* [Fonov et al. (2009), RRID:SCR\_008796; TemplateFlow ID: MNI152NLin2009cAsym], *FSL’s MNI ICBM 152 non-linear 6th Generation Asymmetric Average Brain Stereotaxic Registration Model* [Evans et al. (2012), RRID:SCR\_002823; TemplateFlow ID: MNI152NLin6Asym],

**Functional data preprocessing** For each of the BOLD runs found per subject, the following preprocessing was performed. First, a reference volume and its skull-stripped version were generated using a custom methodology of *fMRIPrep*. Susceptibility distortion correction (SDC) was omitted. The BOLD reference was then co-registered to the T1w reference using `fslirt` (FSL 5.0.9, Jenkinson and Smith, 2001) with the boundary-based registration (Greve and Fischl, 2009) cost-function. Co-registration was configured with nine degrees of freedom to account for distortions remaining in the BOLD reference. Head-motion parameters with respect to the BOLD reference (transformation matrices, and six corresponding rotation and translation parameters) are estimated before any spatiotemporal filtering using `mcflirt` (FSL 5.0.9, Jenkinson et al., 2002). The BOLD time-series (including slice-timing correction when applied) were resampled onto their original, native space by applying the transforms to correct for head-motion. These resampled BOLD time-series will be referred to as *preprocessed BOLD in original space*, or just *preprocessed BOLD*. The BOLD time-series were resampled into standard space, generating a *preprocessed BOLD run in MNI152NLin2009cAsym space*. First, a reference volume and its skull-stripped version were generated using a custom methodology of *fMRIPrep*. Automatic removal of motion artifacts using independent component analysis (ICA-AROMA, Pruim et al., 2015) was performed on the *preprocessed BOLD on MNI space* time-series after removal of non-steady state volumes and spatial smoothing with an isotropic, Gaussian kernel of 6mm FWHM (full-width half-maximum). Corresponding “non-aggressively” denoised runs were produced after such smoothing. Additionally, the “aggressive” noise-regressors were collected and placed in the corresponding confounds file. Several confounding time-series were calculated based on the *preprocessed BOLD*: framewise displacement (FD), DVARS and three region-wise global signals. FD was computed using two formulations following Power (absolute sum of relative motions, Power et al. (2014)) and Jenkinson (relative root mean square displacement between affines, Jenkinson et al. (2002)). FD and DVARS are calculated for each functional run, both using their implementations in *Nipype* (following the definitions by Power et al., 2014). The three global signals are extracted

within the CSF, the WM, and the whole-brain masks. Additionally, a set of physiological regressors were extracted to allow for component-based noise correction (*CompCor*, Behzadi et al., 2007). Principal components are estimated after high-pass filtering the *preprocessed BOLD* time-series (using a discrete cosine filter with 128s cut-off) for the two *CompCor* variants: temporal (tCompCor) and anatomical (aCompCor). tCompCor components are then calculated from the top 2% variable voxels within the brain mask. For aCompCor, three probabilistic masks (CSF, WM and combined CSF+WM) are generated in anatomical space. The implementation differs from that of Behzadi et al. in that instead of eroding the masks by 2 pixels on BOLD space, the aCompCor masks are subtracted a mask of pixels that likely contain a volume fraction of GM. This mask is obtained by thresholding the corresponding partial volume map at 0.05, and it ensures components are not extracted from voxels containing a minimal fraction of GM. Finally, these masks are resampled into BOLD space and binarized by thresholding at 0.99 (as in the original implementation). Components are also calculated separately within the WM and CSF masks. For each CompCor decomposition, the  $k$  components with the largest singular values are retained, such that the retained components' time series are sufficient to explain 50 percent of variance across the nuisance mask (CSF, WM, combined, or temporal). The remaining components are dropped from consideration. The head-motion estimates calculated in the correction step were also placed within the corresponding confounds file. The confound time series derived from head motion estimates and global signals were expanded with the inclusion of temporal derivatives and quadratic terms for each (Satterthwaite et al., 2013). Frames that exceeded a threshold of 0.5 mm FD or 1.5 standardised DVARS were annotated as motion outliers. All resamplings can be performed with *a single interpolation step* by composing all the pertinent transformations (i.e. head-motion transform matrices, susceptibility distortion correction when available, and co-registrations to anatomical and output spaces). Gridded (volumetric) resamplings were performed using `antsApplyTransforms` (ANTs), configured with Lanczos interpolation to minimize the smoothing effects of other kernels (Lanczos, 1964). Non-gridded (surface) resamplings were performed using `mri_vol2surf` (FreeSurfer).

Many internal operations of *fMRIPrep* use *Nilearn* 0.6.2 (Abraham et al., 2014b, RRID:SCR.001362), mostly within the functional processing workflow. For more details of the pipeline, see the section corresponding to workflows in *fMRIPrep*'s documentation.

**Copyright Waiver** The above boilerplate text was automatically generated by *fMRIPrep* with the express intention that users should copy and paste this text into their manuscripts *unchanged*. It is released under the CC0 license.

## B Results

### B.1 Data randomization test

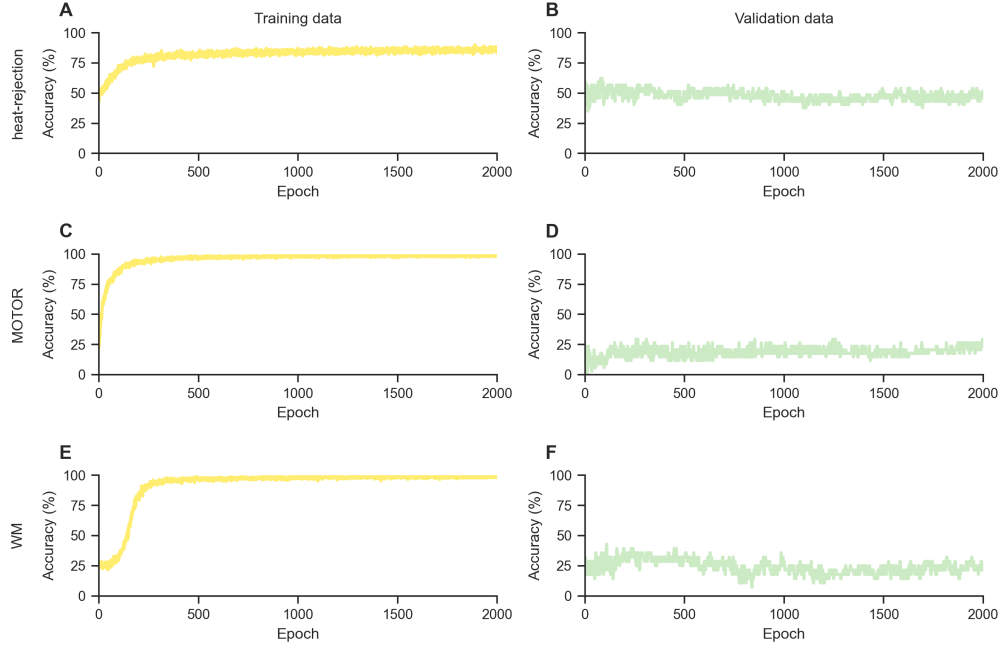


Figure A1: Model performances in the data randomization test. We trained one DL model, according to each dataset’s model configuration (see section 2.1 of the main text), on a variant of each dataset with permuted mental state labels. A,C,E: All models learn to decode the randomized mental state labels well in the training data over the course of 2,000 training epochs. B,D,F: Yet, the models perform close to chance in decoding the randomized labels from the validation data, indicating that the models learned to memorize the mapping between trial-level BOLD maps and mental state labels of the training data. As in the other analyses, we randomly separated each dataset’s training data into new distinct training and validation datasets, comprising 95% and 5% of the data respectively. Colors indicate training (yellow) and validation (green) data. Lines indicate decoding accuracies over the course of training.